Research Article

Boolean-Based Surface Procedure for the External Heat Transfer Analysis of Dams during Construction

Yu Hu, Zheng Zuo, Qingbin Li, and Yunling Duan

State Key Laboratory of Hydroscience and Engineering, Department of Hydraulic Engineering,
Tsinghua University, Beijing 100084, China

Correspondence should be addressed to Zheng Zuo; zuozheng.thu@gmail.com

The external heat transfer of dams during construction is complex because such transfer is location specific and time varying. An external thermal model is developed in this paper. Five types of external heat flux are considered in the mathematical model: air-side convection, electromagnetic radiation, absorbed solar input, water-side convection, and surface insulation effect. A method for extracting and classifying the external surfaces of dams on the basis of Boolean operations is proposed. Heat transfer conditions can be automatically set up for each step according to the proposed method, and the method can be used as a preprocessing facility for finite element analysis. A 285 m high arch dam in Southwest China is examined as a study case. The model is implemented and found to correctly identify different types of external surfaces. Simulation result agrees well with the monitored temperatures.

1. Introduction

Concrete is the most widely used building material in the world. Rough statistics [1] show that over two billion ton quantities of concrete are produced all over the world per year. Temperature plays an important role in the construction of concrete structures [2]. Considerable heat is released during the hydration reaction of young-age concrete. This heat results in temperature gradients near the structure surface because of external heat transfer under varying atmospheric conditions. A large volume of concrete increases the gradients and increases the risk of thermal-stress-induced cracks [3], thereby decreasing the long-term strength and durability of concrete. Thus, developing an appropriate thermal analysis method for concrete, particularly for mega structures (e.g., concrete dams), during the construction phase is essential and necessary.

A dam comprises an extremely large amount of concrete and is referred to as a typical case of massive concrete. To complete this colossal project, the structure must be divided into numerous blocks cast at different times. The entire construction usually requires a number of years to complete, which means that the climate condition changes with seasonal variation during the construction phase. A good example would be the construction of the famous Three Gorges Dam, which took a total of 14 years to complete 27.2 million cubic meters of concrete [4].

The boundary conditions should be consistent with the practical situation to ensure the accuracy of simulating the heat transfer problem. However, the setup work poses difficulty in simulating large and complex structures such as concrete dams. On one hand, the dam is bounded by a group of surfaces, which are subjected to various external thermal conditions. On the other hand, the dam constantly grows with the gradually changing boundary surfaces. Therefore, external thermal conditions are location specific and time varying, which makes the selection and setup of the boundary conditions complex. The surfaces of different steps are manually chosen in conventional thermal simulations, which is a tedious and time-consuming task that does not guarantee absolute accuracy.

A number of experimental and numerical studies on the external heat transfer problem of concrete were conducted. For instance, Demir [5] investigated the natural

convection temperature/velocity field around a horizontal concrete cylinder that is heated with a heat source. Lee et al. [6] conducted an experiment to investigate the convective heat transfer coefficient during the hydration process. G. F. Jones and R. W. Jones [7] studied a heat transfer problem for an insulated and reinforced concrete wall, in which the surface boundary is solved by using Newton's cooling law. However, these studies mainly focused on stable laboratory test conditions where the external heat transfer boundary condition is relatively simple.

Much effort was given to study the external heat transfer of dams. Léger and Seydou [8] and Léger and Leclerc [9] investigated the 1D/2D temperature field of some dams during the operating phase. Sheibany and Ghaemian [10] intensively studied the environmental effect of heat transfer in arch dam engineering but failed to consider the surface insulation effect. In another study, Jin et al. [11] investigated the solar effect on exposed dam surfaces during the operating phase. However, the objects of these studies were dams that had already been built; that is, the dams were already under the postconstruction or operation phase, where the situation of the external surface boundary regions barely changes.

The finite element (FE) method is widely used to simulate the thermal problem of dams during the construction phase. Numerous relevant studies address the FE method [2, 12–21]. Cervera et al. [12] translated a 3D thermal problem into a 1D/2D FE analysis problem by simplifying the longitudinal direction. Wu and Luna [2] and Luna and Wu [15] studied the numerical implementation of the thermal stress problem in roller-compacted concrete (RCC) dams without considering solar and electromagnetic radiation. Saetta et al. [16] proposed the constituting factors of the external thermal flux. However, they did not discuss exact estimation methods. Noorzaei and Bayagoob [18, 19] simulated RCC dams that are under construction to study wind and solar effects. However, the solar input in their study was simplified to a constant.

The numerical thermal simulation of dams had been studied, but the setup problem of the external boundary conditions at each step was not technically discussed. Limited studies focus on the preliminary procedure of external surfaces for the external heat transfer of dams. Therefore, this study presents a method for the automatic setup of external heat transfer boundaries during the analysis of the entire construction phase. The external heat transfer of dams is classified, and the basic mathematical model is established. Boolean-based algorithms are proposed to extract different types of external surfaces and to set appropriate heat transfer conditions. A super-high arch dam is examined as a study case by using the developed program to test the automatic method in practical engineering applications.

2. Mathematical Model

The governing equation of 3D unsteady heat transfer can be derived from the energy conservation principle and the Fourier law of heat conduction, which is written as follows:

$$\rho C_p \frac{\partial T}{\partial \tau} = \left(\lambda_x \frac{\partial^2 T}{\partial x^2} + \lambda_y \frac{\partial^2 T}{\partial y^2} + \lambda_z \frac{\partial^2 T}{\partial z^2} \right) + f, \qquad (1)$$

where T is the temperature; λ is the thermal conductivity, which is always considered isotropic in concrete material; that is, $\lambda = \lambda_x = \lambda_y = \lambda_z$; f is the internal heat source produced per volume, homogeneously distributed over the concrete. f generally consists of two main parts: hydration heat generation and the cooling effect of embedded coolpipes, which was investigated in our previous work [14, 17, 20].

Massive concrete has complex boundary conditions during the construction phase. The external heat transfer of the boundary surfaces can generally be expressed as

$$q = \lambda \frac{\partial T}{\partial n} = f\left(q_c, q_r, q_a, q_w, q_p\right), \qquad (2)$$

where n is the normal direction of the external surfaces and q is the external heat flux, which is a combination of five components. These components are discussed in detail in this section. Various combinations are applied in different surface areas to simulate a dam during construction. The rule of the combination setup is presented in detail in Section 4.

2.1. Air-Side Convection. Heat convection occurs upon exposed concrete surfaces because of the bulk motion of air fluids that carry and disperse the heat [22]. The air-side convective flux q_c is proportional to the temperature difference between the concrete and the surrounding air. Heat convection can be given by using Newton's law of cooling or by using the Robin boundary condition:

$$q_c = h_c \left(T - T_a\right), \qquad (3)$$

where T_a denotes the ambient temperature and h_c denotes the convective coefficient, which is considered constant in some previous studies on dams [2, 11, 14]. However, the convective coefficient is actually affected by numerous factors, among which wind speed was highlighted in recent studies as the major factor [23, 24]. The thermal simulation of dams should consider this wind effect because dams are commonly built in canyons where wind is naturally strong. Nusselt-Jürges correlation [23], a well-established form of convective coefficient that considers wind speed, is used in this paper and can be defined as

$$h_c = 5.678 \left\{ a + b \left[\left(\frac{294.26}{T_a^{[K]}} \right) \frac{V_w}{0.3048} \right]^m \right\}, \qquad (4)$$

where V_w is the wind speed; a, b, and m are the parameters to be decided based on the applied condition; $T_a^{[K]}$ is notably the degree Kelvin of ambient temperature. The following equation gives the conversion formula based on degree Celsius:

$$[K] = [°C] + 273.15. \qquad (5)$$

Air temperature always varies and hardly remains constant even throughout a single day. In this work, the T_a of each step is used as the mean temperature over the increment of time. Constantly recording the ambient temperature is impractical; thus, we use the daily mean temperature to represent the entire day for convenience. We can employ
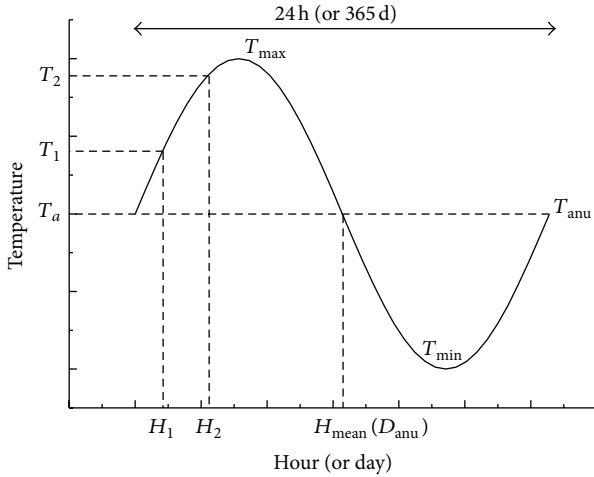
FIGURE 1: Ambient temperature sinusoid curve for one day (or one year).

a sinusoid function [25] curve with a period of 24 h for typical temperature history (see Figure 1). The mean daily temperature can be fit with two measured temperatures T_1 and T_2 at times H_1 and H_1 by using the following equation:

$$T_a = \frac{T_1 - (T_2 - T_1) \sin\left[(H_1 - H_{Mean})\pi/12\right]}{\sin\left[(H_2 - H_{Mean})\pi/12\right] - \sin\left[(H_1 - H_{Mean})\pi/12\right]}, \tag{6}$$

where H_{Mean} is the middle time between the peak and valley. When the record time is at the middle time such as $\tau_1 = \tau_{mean}$, the temperature measured at that time can be directly considered the mean temperature; that is, $T_a = T_1$.

Unfortunately, recording or accessing detailed local weather data in some engineering projects is difficult and cannot be guaranteed even though only one temperature measurement per day is taken. That implies that daily temperatures cannot be determined from (6). We can apply the following sinusoidal curve to approximate T_a over the entire year:

$$T_a(D) = 0.5(T_{Max} - T_{Min}) \sin\left[\frac{2\pi(D - D_{Anu})}{365}\right] + T_{Aun}, \tag{7}$$

where D denotes the day of the year (e.g., 1 for January 1st and 32 for February 1st).

2.2. Exposed Radiation to Environment. Electromagnetic energy is constantly emitted by concrete through exposed surfaces and can be calculated by using the Stefan-Boltzmann law:

$$q_r = F_r \sigma \left[\left(T^{[K]}\right)^4 - \left(T_a^{[K]}\right)^4 \right], \tag{8}$$

where F_r is the emissivity of the surface and $\sigma = 5.670373 \times 10^{-8}$ W m^{-2}K^{-4}, which is referred to as the Stefan-Boltzmann constant [26]. The temperatures applied in (8) should notably be used in degree Kelvin.

2.3. Absorbed Radiation from the Sun. Solar radiation was not considered in numerous thermal studies on dams [2, 14, 15]. A recent work [11] showed that irradiation has a great thermal effect on the exposed surfaces of a dam. Proper calculation of the absorbed solar radiation of the structure surface is complex because of considerations such as the sun's position, environmental factors, and surface conditions.

The revolution orbit and rotation circle of the earth are not on the same plane because the equatorial plane tilts at an angle of 23.45° to the orbital plane. Solar declination δ, which is defined as the angle between the earth-sun line and the equatorial plane, consequently varies from 0° to 23.45° during one period of revolution (see Figure 2). The daily declination is obtained through approximation throughout a year as

$$\delta = 23.45° \sin\left(360° \frac{D + 284}{365}\right), \tag{9}$$

where D is the day of year. The equation shows that if $81 < D < 263.5$ then $\delta > 0$, which is the time when the earth-sun line crosses the Northern Hemisphere, namely, the summer time for the Northern Hemisphere.

Figures 2 and 3 show the position map of the sun and the structure surface of the earth. The relation among these angles through a 3D geometry deduction can be written as

$$\sin \beta = \cos L \cos \delta \cos H + \sin L \sin \delta, \tag{10}$$

$$\sin \phi = \frac{\sin H \cos \delta}{\cos \beta}, \tag{11}$$

$$\cos \phi = \frac{\cos H \cos \delta \sin L - \sin \delta \cos L}{\cos \beta}, \tag{12}$$

$$\gamma = \phi - \psi, \tag{13}$$

$$\cos \phi = \cos \beta \cos \gamma \sin \mu + \sin \beta \cos \mu, \tag{14}$$

where H is the hour angle (the detailed calculation of this variable is tallied in the appendix); L is the latitude value (in degrees: positive for the northern site and negative for the southern site); μ is the inclination angle of the structure surface; θ is the angle of incidence, which is the angle between the earth-sun line and the line normal to the surface; ψ is the surface azimuth, which is defined as the angular displacement from the south direction to the normal direction of the structure surface on the horizontal plane; β is the solar altitude angle, which represents the angle between the horizontal plane and the emanating line from the sun; γ is the surface-solar azimuth angle; ϕ is the solar azimuth angle.

We can obtain the exact values of $L, H, \delta, \psi,$ and μ for a specific time on a specific location on earth. Then, β can be calculated by (10), ϕ can be found by (11) and (12), and θ is determined by (14). So far, all the solar angles involved in the irradiation computation are obtained. When $H = 0$, β notably reaches the daily maximum angle of $\pi/2 - |L - \delta|$, which is the moment called the *solar noon*.

When the sun's position and solar angles are determined as described, we can calculate the total solar energy input
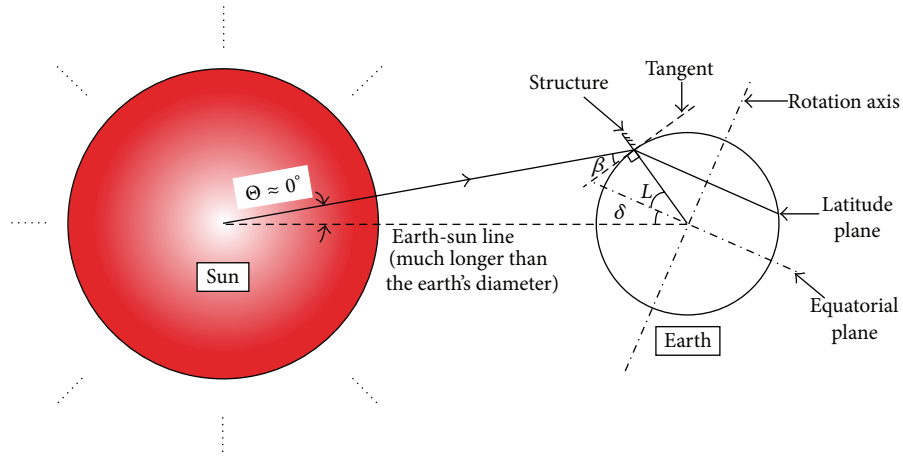
FIGURE 2: Positions of the Sun and the Earth (this figure shows a winter time for the north because the Earth–Sun line crosses the Southern Hemisphere).
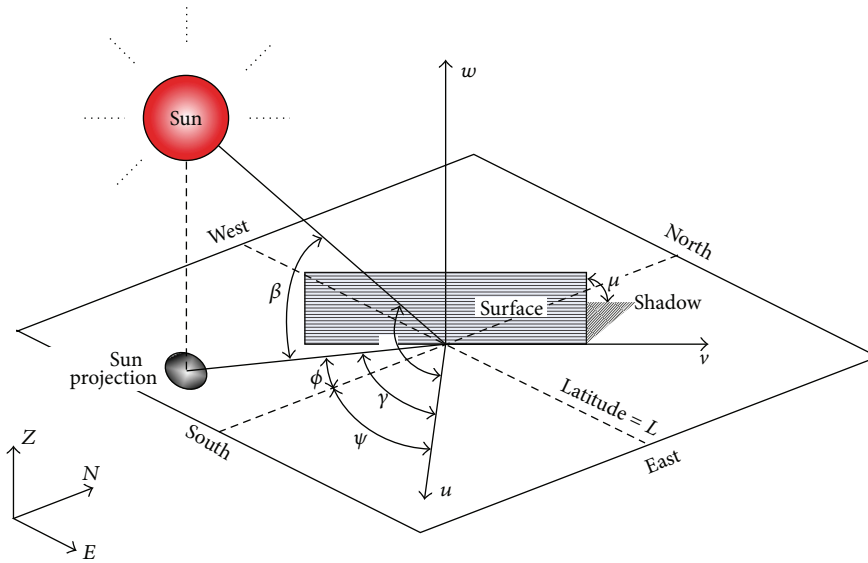

FIGURE 3: Solar angles involved for a structure surface.

that strikes the structure surface. This energy input can be measured by using three components:

$$E_{\text{Sun}} = Y_{\text{Beam}} E_{\text{Beam}} + Y_{\text{Diff}} E_{\text{Diff}} + E_{\text{Refl}}, \tag{15}$$

where E_{Beam}, E_{Diff}, and E_{Refl} represent the beam (direct), diffuse, and ground reflector components of solar radiation from the sky dome and Y_{Beam} and Y_{Diff} represent the irradiation coefficient, considering the surface angle. These components can be obtained through mathematical and geometry relations with the extraterrestrial solar radiation from a clear-sky model proposed by ASHRAE [27]:

$$E_{\text{Beam}}$$
$$= E_0 \exp\left(-\eta_{\text{Beam}} \ m^{1.219 - 0.043\eta_{\text{Beam}} - 0.151\eta_{\text{Diff}} - 0.204\eta_{\text{Beam}}\eta_{\text{Diff}}}\right), \tag{16}$$

$$Y_{\text{Beam}} = \max\left(\cos\theta, 0\right), \tag{17}$$

$$E_{\text{Diff}}$$
$$= E_0 \exp\left(-\eta_{\text{Diff}} \ m^{0.202 + 0.852\eta_{\text{Beam}} - 0.007\eta_{\text{Diff}} - 0.357\eta_{\text{Beam}}\eta_{\text{Diff}}}\right), \tag{18}$$

$$Y_{\text{Diff}} = \Big[\max\left(0.45, 0.55 + 0.437\cos\beta\cos\gamma \right.$$
$$\left. + 0.313\cos^2\beta + \cos^2\gamma\right)\Big] \sin\mu\cos\mu, \tag{19}$$

$$E_{\text{Refl}} = \frac{1 - \cos\mu}{2} g\left(E_{\text{Beam}} \sin\beta + E_{\text{Diff}}\right), \tag{20}$$

where E_0 is the extraterrestrial solar radiant flux, m is the relative air mass, η is the parameter that represents optical depths, and g is the ground reflectance of the foreground. These four parameters can be investigated as described in the following paragraphs.

The extraterrestrial solar radiant flux E_0 varies throughout the year owing to the slightly elliptical orbit path, which can be given by

$$E_0 = E_{sc} \left\{ 1 + 0.033 \cos \left[360° \frac{(D-3)}{365} \right] \right\}, \quad (21)$$

where $E_{sc} = 1367 \, \text{W/m}^2$ and is referred to as the solar constant [28].

The relative air mass m represents the ratio of the actual air mass to the air mass with the sun shining directly overhead. m can be considered a function of the solar altitude angle β [29] as follows:

$$m = \frac{1}{\sin \beta + 0.50572(6.07995 + \beta)^{-1.6364}}. \quad (22)$$

The ground reflectance g depends on the reflectance capability of the foreground near the site, ranging from 0 to 1. Several reflectance parameters of typical landforms were listed in a previous study [30], where water and dry ground were 0.07 and 0.20, respectively.

The parameters that represent the optical depths η_{Beam} and η_{Diff} are location specific, and the data from 11,124 stations worldwide can be found in the ASHRAE handbook [27].

In terms of reaching solar energy E_{Sun}, the structure surface would absorb a part of this energy while reflecting the rest. The absorbed energy can then yield a correlation expression as

$$q_a = \zeta E_{\text{Sun}}, \quad (23)$$

where the scale factor ζ is the absorptivity of the exposed surface.

Solar radiation input occurs only during daytime with a clear sky. q_a is small during night and rainy days and can be neglected. In engineering applications, the daily energy can be summed up on the basis of the hourly E_{Sun} value:

$$q_a(D) = \zeta \sum_{H=H_{\text{Rise}}}^{H_{\text{Set}} - H_{\text{Rise}}} E_{\text{Sun}}(H) = \zeta \overline{E_{\text{Sun}}} \left(H_{\text{Set}} - H_{\text{Rise}} \right), \quad (24)$$

where H_{Rise} and H_{Set} denote the sunrise and sunset hours, respectively, and $\overline{E_{\text{Sun}}}$ denotes the time average value of E_{Sun} during daytime.

2.4. Water-Side Convection.

Several dams begin to fill the reservoir during the construction phase to improve the performance of power production, which results in the concrete exchanging heat with the reservoir through the water-side surface below the reservoir level. This phenomenon is considered a convection boundary with liquid fluid, which can also be described in Newton's law of cooling:

$$q_w = h_w (T - T_w), \quad (25)$$

where T_w denotes the water temperature and h_w denotes the convection coefficient between the concrete and water. Coefficient h_w is relatively large for water-side convection

unlike that for air-side convection. The water-side convection coefficient is 20 times to 1000 times that of the air-side convection [31, 32]. In this situation, the boundary can be directly dealt as a Dirichlet boundary condition (first-type boundary condition):

$$T = T_w. \quad (26)$$

In engineering applications, T_w can be obtained by monitoring the water temperature or through the empirical prediction method [33, 34].

2.5. Surface Protection.

The concrete surface may be covered with insulation protections during construction to prevent thermal cracks induced by atmospheric temperature shock. Materials with high thermal resistances, such as cotton quilts, polystyrene foam plastic (PFP) [35] boards, and sprayed polyurethane, are ideal options for protection in engineering applications. Figure 4 shows two typical thermal protections used in dams. Tiling the cotton quilt on horizontal surfaces, such as the top faces of new-cast lifts, is convenient. And polystyrene foam boards are suitable for pasting clung to the nonhorizontal surfaces. We can consider the boundary condition as a composite wall comprising miscellaneous materials in a series. Similar to the air-side convection, we can apply the following Robin boundary condition:

$$q_p = h_p (T - T_a), \quad (27)$$

where h_p denotes the equivalent convection coefficient of the protection series and is given as the reciprocal of the sum of thermal resistances:

$$h_p = \frac{1}{1/h_c + \sum b_p / \lambda_p}, \quad (28)$$

where h_c denotes the nonprotective convective coefficient in a nonwind condition ($V_w = 0$ in (4)), b_p denotes the width of each protection, and λ_p denotes the thermal conduction coefficient of each insulation layer.

3. Finite Element Methods

Solving (1) through analytical methods with the aforementioned geometrically complex dam structures and various boundary conditions is impractical. The FE method, which is the most widely applied numerical tool in engineering fields, is chosen as the numerical approach to solve the heat transfer problem of the dam under construction in this study.

The 3D space V can be subdivided into numerous elements. Let T^e be the temperature of an arbitrary location within an element, which can be interpolated as a function of the nodal temperatures on this element mesh:

$$T^e = [N] \{T\}^e, \quad (29)$$

where $\{T\}^e$ denotes the nodal temperature arrays and $[N]$ denotes the interpolation function matrix. We can also transpose (29) into (1). The classic FE formulation can be formed as

$$[C] \left\{ \frac{\partial T}{\partial \tau} \right\} + [K] \{T\} = \{Q\}, \quad (30)$$
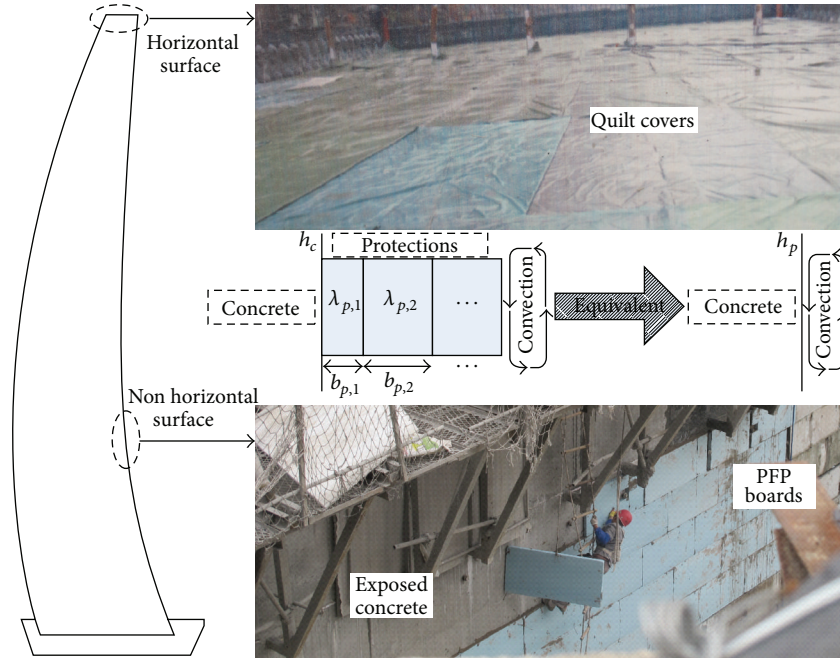
FIGURE 4: Surface protection and its equivalent model.

where $[C]$ and $[K]$ denote the heat capacity and thermal conductivity matrices, respectively and $\{Q\}$ denotes the heat flux vector:

$$[C] = \rho C_P \int_V [N]^T [N] \, dV, \tag{31}$$

$$[K] = \rho C_P \int_V [M]^T \lambda [M] \, dV, \tag{32}$$

$$\{Q\} = \int_V [N]^T f \, dV, \tag{33}$$

where $[M]$ is the derived form of $[N]$.

Given the boundary conditions mentioned in (2), $\{Q\}$ can be rewritten as

$$\{Q\} = \int_V [N]^T f \, dV + \int_{\Gamma_c} [N]^T q_c \, d\Gamma_c + \int_{\Gamma_r} [N]^T q_r \, d\Gamma_r$$
$$+ \int_{\Gamma_a} [N]^T q_a \, d\Gamma_a + \int_{\Gamma_w} [N]^T q_w \, d\Gamma_w + \int_{\Gamma_p} [N]^T q_p \, d\Gamma_p, \tag{34}$$

where Γ represents the external surface regions, which have various types. The method of determining the different types of surface regions at different times is proposed in Section 4.

Equation (30) yields the following expression with the help of the backward difference scheme through the discretization of the time dimension:

$$\left(\frac{1}{\Delta\tau} [C] + [K] \right) \{T\}_{\text{inc}} = \{Q\}_{\text{inc}} + \frac{1}{\Delta\tau} [C] \{T\}_{\text{inc}-1}, \tag{35}$$

where $\Delta\tau$ denotes the increment time and the subscript inc is the time increment. The initial condition and thermal boundary conditions are known. The temperature field of any time can be deduced increment by increment.

4. Boolean-Based Surface Procedure

The external heat transfer conditions during the construction phase of a large dam are complex. For a proper FE analysis of a dam under construction, the casting of a new lift means activating the lift elements, which changes the external surface regions. In some large projects, the dam is composed of thousands of lifts, which makes the manual selection of different types of surfaces at each step impractical. Therefore, an automatic surface extracting and taxonomy method based on Boolean operations is presented in this study.

4.1. Boolean Operations. Boolean operations are a group of symbolic computation rules used to operate polygons. Three basic operations are always conducted as illustrated in Figure 5: intersection, union, and difference. In the programming of a Boolean-based operation between two surface sets (e.g., M and N), two labels m and n are attached on each surface element. If the element belongs to the set M, $m = 1$; otherwise, $m = 0$. Similarly, $n = 1$ refers to the elements in the internal area of N. Therefore, the rules of the Boolean-based operation can be defined as follows.

(i) Intersection: it is denoted as $M \wedge N$, which generates the set of elements located in the area where M and N overlap. This rule means that the sets are the elements with $m + n = 2$.

(ii) Union: it is denoted as $M \vee N$, which generates the set of overall elements, which is a member of M, N, or both. This rule means that the sets are the elements with $m + n \geq 1$.

(iii) Difference: it is denoted as $M - N$, which generates the set of elements located where M remains when N

(1) Read surface sets already been defined, S_1, S_2, S_3 and S_4, according to Section 4.2.
(2) Detect outlet hole surfaces in the dam body, and store them as S_5, according to Algorithm 3.
(3) Detect joint surfaces between adjacent monoliths, and store them as S_6, according to Algorithm 3.
(4) Detect foundation surfaces between dam and rock, and store them as S_rock, according to Algorithm 3.
(5) Kill all the dam elements.   // the elements whose $lift\_ID > 0$.
(6) **for** $i = 1, 2, \ldots, steps$ **do**
(7)   Activate the lift cast at this step.   // the elements whose $lift\_ID = i$.
(8)   Recognize external surfaces of activated elements, store them as S_all according to Algorithm 2.
(9)   Look for the element surfaces with $lift\_ID = i$ from S_all, and note them as S_lift.
(10) $S\_rock = S\_rock \wedge S\_all$.
(11) $S\_up = (S\_lift \wedge S_3) \vee S\_up$.
(12) $S\_down = (S\_lift \wedge S_4) \vee S\_down$.
(13) $S\_joint = S_6 \wedge S\_all$.
(14) $S\_hole = S_5 \wedge S\_all$.
(15) $S\_top = S\_all - S\_up - S\_down - S\_joint - S\_hole$.
(16)   Set boundary conditions according to Table 2
(17)   Seek the highest elevation z of nodes in the latest cast lift, which is noted as z_h.
(18) $z\_mono \ [mono\_ID \ [i]] = z\_h$.   // change the top elevation of the new-rise monolith.
(19)   **for** $j = 1, 2, \ldots, incs \ [i]$.   // increments of this step
(20)   Finite element solver.
(21)   **end loop** j.
(22) **end loop** i.

ALGORITHM 1: Boolean-based surface procedure.

TABLE 1: Predefined variables.

Variables	Dependence	Note
$lift\_ID$	Element dependent	The label of the casting sequence and $lift\_ID = 0$ represent the nonconcrete elements (i.e., rock base).
$mono\_ID$	Lift dependent	The variable represents the monolith to which the lift belongs, and $mono\_ID \ [0] = 0$.
z_mono	Monolith dependent	The variable represents the highest elevation of each monolith during construction, where all variables are initially set as 0.

is substracted. This rule means that the sets are the elements with $m - n = 1$. Similarly, $n - m = 1$ yields the result of the $N - M$ operation.

4.2. Preliminary Defining Surfaces.

Four simple preliminary surface groups should be identified to obtain precisely different types of external surfaces in the simulation. Figure 6 shows the preliminary surface groups of a typical arch dam layout.

(i) Model-side surfaces: the in-rock boundary surfaces of the model should be identified and noted as S_1.

(ii) Dam-top surfaces: the top surfaces of the dam body should be identified and noted as S_2, and usually those surfaces are on the same elevation.

(iii) Upstream surfaces: the upstream surfaces of the dam should be identified and noted as S_3.

(iv) Downstream surfaces: the downstream surfaces of the dam should be identified and noted as S_4.

Death/rebirth technology is used to simulate the construction process in FE analysis. The entire analysis is divided into numerous steps on the basis of the casting-time plan. The lift elements are activated at the beginning of each step. A $lift\_ID$ variable is created for each element to store the lift casting sequence. Two additional arrays are used to represent the space relations, as shown in Table 1.

4.3. Surface Procedure and FEM Implementation.

We are now ready to present the surface extraction and taxonomy procedures based on Boolean operations. First we set a nomenclature rule of the surface group identification. (1) Postfix including integer numbers are the surfaces remain the same during the analysis, or we can name them as static surfaces, like S_1, S_2, and so forth. (2) Postfix including characters are the surfaces change during the analysis, or we can name them as dynamic surfaces, like S_up, S_down, and so forth. The pseudo-code description of the procedure can be summarized by the following algorithm.

Various types of external heat transfer occur on different surfaces during construction. More than one type of heat transfer may co-exist on one surface. The surfaces stored in Algorithm 1 are an efficient taxonomy method for each step. We can set the boundary condition as summarized in Table 2.
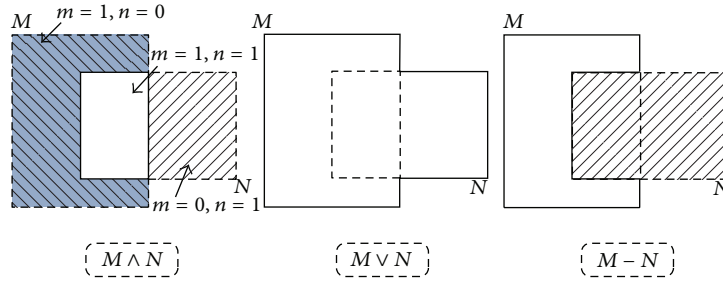
FIGURE 5: Surface Boolean operations.

TABLE 2: External surface taxonomies for boundary conditions setup.

| Surface region		Combination of boundary conditions
In-rock boundary surfaces	S_1	$q(\tau) = 0 \ (z > z_g)$ $T(\tau) = T_g \ (z \leq z_g)$
Rock-exposed surfaces	S_rock	$q(\tau) = q_c + q_r + q_a$
Upstream surfaces	S_up	$q(\tau) = \begin{cases} q_c + q_r + q_a & (z > z_{up}, p(\tau) = 0) \\ q_p & (z > z_{up}, p(\tau) = 1) \\ q_w & (z \leq z_{up}) \end{cases}$
Downstream surfaces	S_down	$q(\tau) = \begin{cases} q_c + q_r + q_a & (z > z_{down}, p(\tau) = 0) \\ q_p & (z > z_{down}, p(\tau) = 1) \\ q_w & (z \leq z_{down}) \end{cases}$
Joint surfaces	S_joint	$q(\tau) = \begin{cases} q_c + q_r + q_a & (p(\tau) = 0) \\ q_w & (p(\tau) = 1) \end{cases}$
Top surfaces	S_top	$q(\tau) = \begin{cases} q_c + q_r + q_a & (p(\tau) = 0) \\ q_p & (p(\tau) = 1) \end{cases}$
Outlet hole surfaces	S_hole	$q(\tau) = \begin{cases} q_c + q_r + q_a & (z \geq z\_mono - h\_hole) \\ q_c + q_r & (z_{up} < z < z\_mono - h\_hole) \\ q_w & (z \leq z_{up}) \end{cases}$
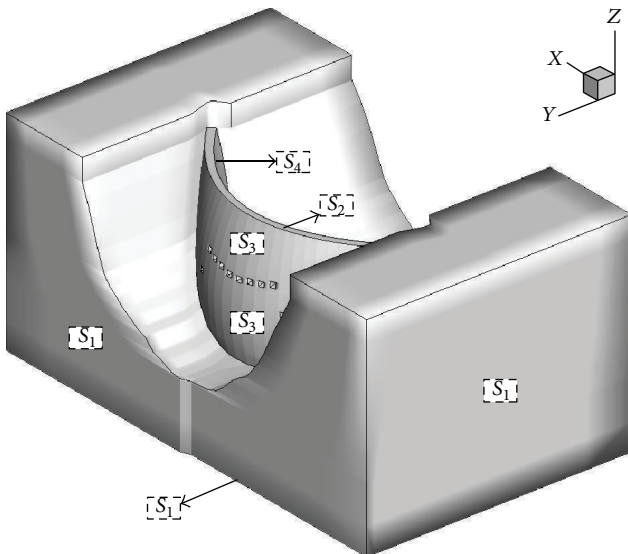
FIGURE 6: Preliminary defined surface groups.

A few remarks should be made on the setup rule in Table 2:

(i) The in-rock vertical surfaces generated by the model-side cutting are adiabatic because the horizontal heat transfer in the infinite rock is symmetrical to these surfaces.

(ii) The ground temperature beneath the upper 6 m of the surface of the Earth maintains a nearly constant temperature between 10°C and 16°C [36], depending on the site latitude. Let Z_g denote the upper level of the constant temperature layer, and the thermal boundaries below Z_g on S_1 can be expressed as the first-type boundary condition.

(iii) Z_{up} and Z_{down} are used to represent the upstream water level and downstream water level, and the impounding plan should be drawn up when making prediction.

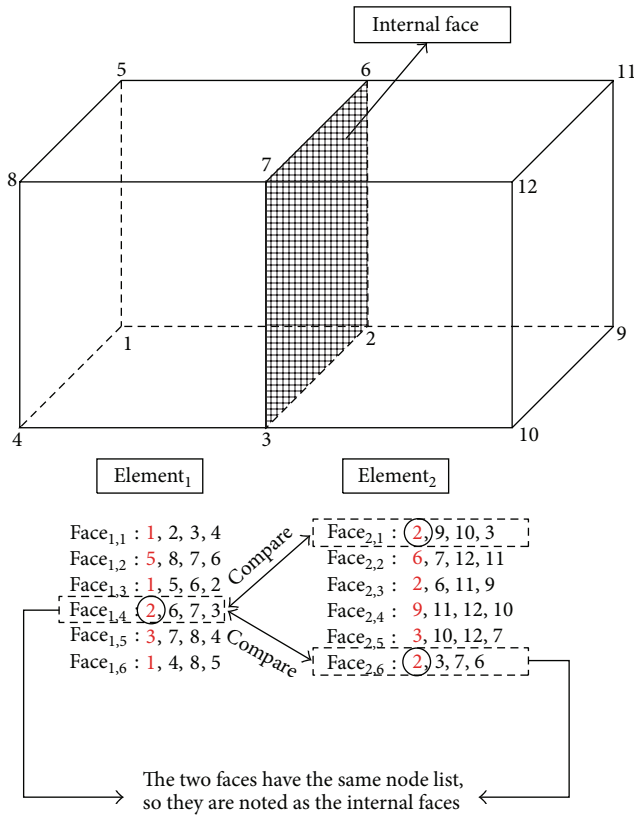(iv) A protection scheme should be established based on the design plan when a prediction is conducted

FIGURE 7: Example of recognizing the inside faces. The red bold number is the minimum node number of the face.

The detection algorithm of S_5, S_6, and S_rock mentioned in Algorithm 1 can be executed in Algorithm 3.

A remark should be noticed that the algorithms can also be applied as a preprocessing facility for a third-party FEM software package. An improvement which should be made on the origin Algorithm 1 is that the surface sets extracted at each step should be separately stored and without executing the FEM solver.

4.4. Software Development. In this study, a user-friendly interface for data input is developed based on the EXCEL software. The embedded VBA programming language can be utilized to provide a convenient user interface and to handle the data automatically. Several forms are generated for users to collect the information required in the simulation, including climate condition, construction procedure, material properties, and predefined surfaces. The form style is concise, explicit, and easy-to-use.

A C-language-based program is compiled to process the data input from the spreadsheet and the FE meshes. Algorithm 1 to Algorithm 3 are implemented in the program.

Several commercial or free source FEM packages exist. Our developed program can be exported as requested provided that the input format is known. In this study, MSC.Marc [37] is used as the third-party FEM solver because of its quickness and stable benchmark.

Common users found the postprocessing module of MSC.Marc to be inconvenient and awkward. A program is developed to decode the .t16 result output file for fast, automatic, and easy-to-use postprocessing. A customized form, which can be found in the EXCEL interface, offers two options: desired nodes and desired contour time. The developed program can then extract and plot the data, including the time-temperature curves and temperature contours.

Figure 8 summarizes the entire flow process.

5. Case Study

5.1. Engineering Description. The site of the Xiluodu hydropower project is located in the lower reach of the Jinsha River, Yunnan Province in Southwest China. The geographic coordinate is $28°13'02''$ N, $103°33'46''$ E. The project is designed as a dome dam that is double curved in both horizontal and vertical planes and with a maximum height of 285.5 m and a crest length of 700 m. The footing sits upon the riverbed foundation on a 324.5 m elevation. A total of 31 monoliths are planted across the river. Seven 12.5 m × 13.5 m surface spillways and eight 6 m × 6.7 m deep outlet holes are arranged in the arch dam body. The transversal section of the dam is curve shaped and is 14 m wide at the crest and 60 m wide at the footing.

5.2. Construction Schedule. The dam started casting concrete in March 2009. The dam comprises about 2100 lifts within an approximately five-year construction period because of considerations for proper concrete casting and to avoid thermal cracks. A total of 1961 lifts were completed by June 2013. The detailed casting-time sequence was recorded.

or based on the actual condition when simulating the past. $p(\tau)$ is the variable that denotes whether protection is covered at time τ. In large engineering projects, $p(\tau)$ is also relevant to the surface locations. Some projects may be dependent on the lift and others on the elevation, in which case $p(\tau, lift\_ID)$ or $p(\tau, z)$ is used to represent the protection status.

(v) h_hole represents the height of the hole. When concrete is cast over the top of the holes, the sun barely shines into the spillway holes constructed inside the dam body; thus, solar irradiation is not considered in these areas.

(vi) q_a differs from all the surfaces because the inclination of every element face is not the same.

Algorithm 1 mentions that the external surfaces should be initially recognized. Each internal face for the FE meshes must have the same node list with only one face of another element. One way to extract the external surfaces is to check all the internal faces by comparing all the faces of the model. However, this method costs too much time for large models. In this study, a minimum node number is used as a label to accelerate the extracting process, the details of which are described in Algorithm 2. Figure 7 shows an example where two elements are adjacent on one internal face.
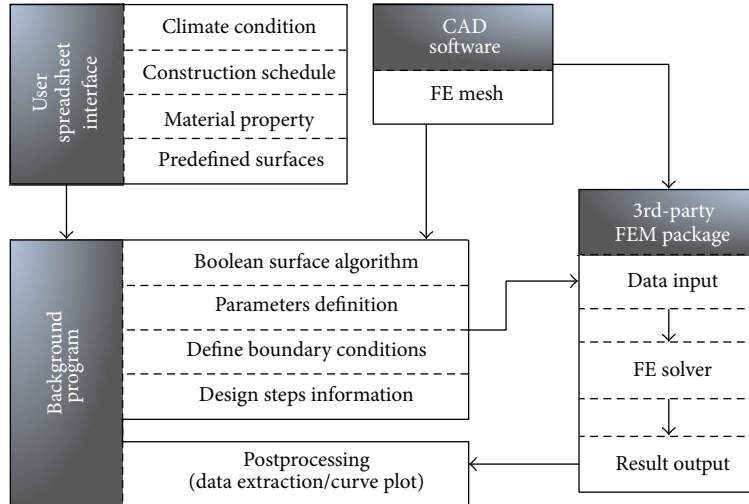
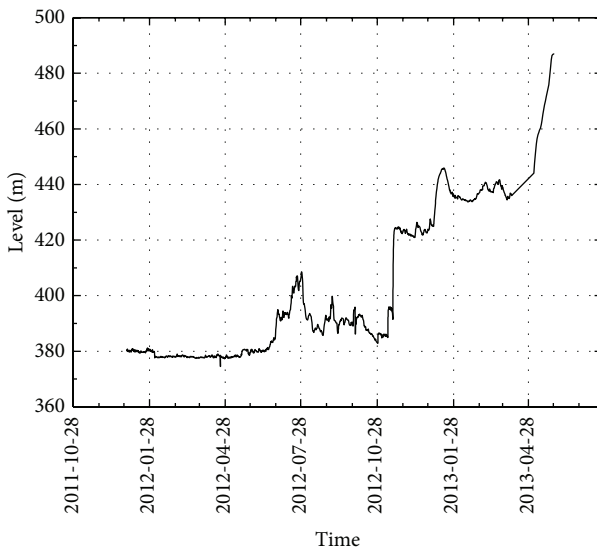FIGURE 8: Flowchart of the software development.

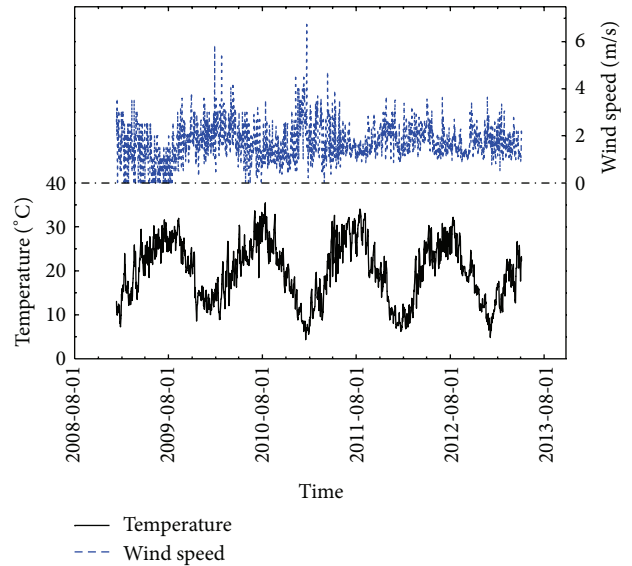
FIGURE 9: Water level process during construction.

FIGURE 10: Weather curve (air temperatures and wind speeds).

The upstream cofferdam was demolished in March 2012, and the reservoir was impounded. The upstream water level was measured and recorded (see Figure 9).

5.3. Climate Conditions. The site is located in a V-shaped canyon of the Jinsha River and is subjected to a subtropical climate. A nearby hydrologic station records the weather data daily. The ambient temperatures and wind speeds from January 2009 to May 2013 are shown in Figure 10, in which the temperatures over the years can be considered repeated sinusoidal curves on the basis of (7).

A meteorological station is located near the dam site in Zhaotong, and the fundamental solar measurement data were used as the reference for the simulation. Table 3 shows the

data for the solar irradiation calculation, which acts as the basic design parameters in the simulation.

Table 3 shows the calculation result of the solar radiation, where E^*_{Beam} and E^*_{Diff} are the radiation values at *solar noon*, $\overline{E_{\text{Beam}}}$ and $\overline{E_{\text{Diff}}}$ are the average radiation value's during daytime, and $\overline{E^V_{\text{Sun}}}$ and $\overline{E^H_{\text{Sun}}}$ are, respectively, the average total solar input for the vertical and horizontal structure surfaces.

η_{Beam} and η_{Diff} are the station measurements, based on which the values of E^*_{Beam} and E^*_{Diff} are calculated by (16) and (18) by setting $H = 0$. H_{Rise} and H_{Set} can then be obtained through a multiple trial computation when β reaches 0°. Averaging E_{Beam}, E_{Diff}, and E_{Sun} from H_{Rise} to H_{Set} yields the result of $\overline{E_{\text{Beam}}}$, $\overline{E_{\text{Diff}}}$, and $\overline{E_{\text{Sun}}}$.
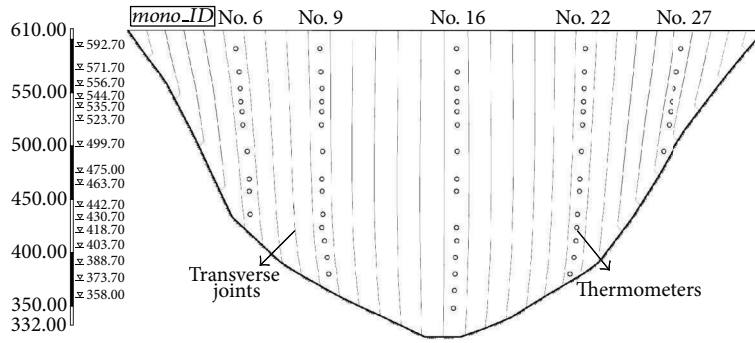
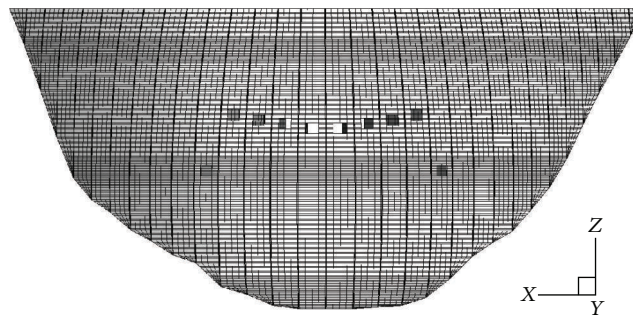FIGURE 11: Instruments setup (viewed from upstream to downstream).

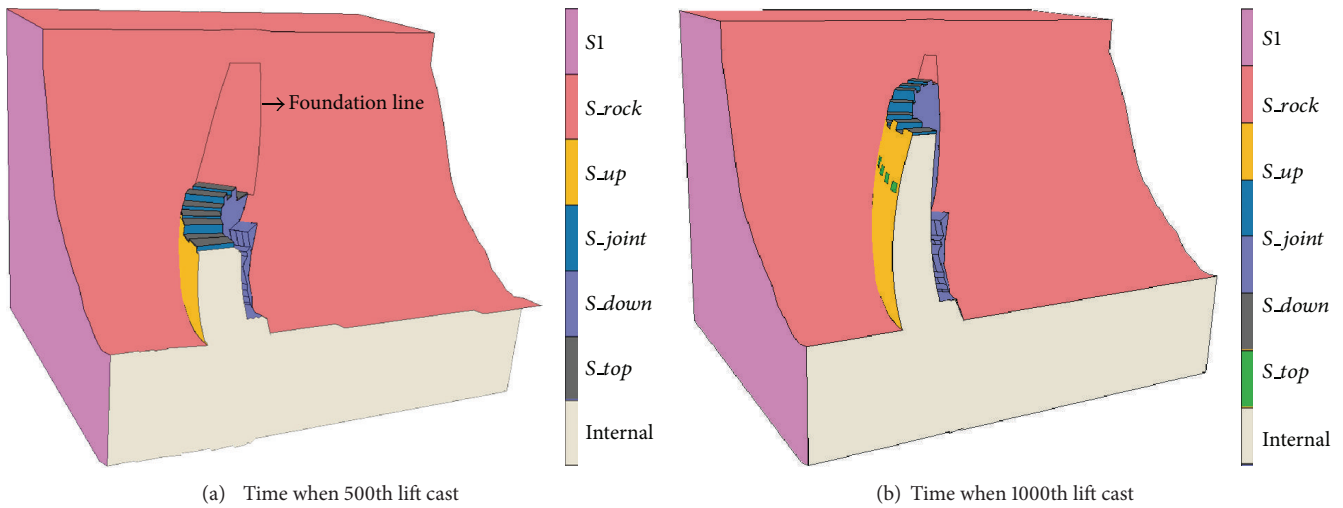FIGURE 12: Finite element meshes of the dam body.

(a) Time when 500th lift cast

(b) Time when 1000th lift cast

FIGURE 13: Sketch of surface taxonomy map.

```
(1)    for i = 1, 2, . . . , num_elements do        // Searching all the elements
(2)            Request the element type and the count of faces in one element is stored as S.
(3)            for j = 1, 2, . . . , S do           // Searching all the faces
(4)                    Obtain the minimum node number of the face nodes, labeled as Node_{i,j}.
(5)            end loop j
(6)    end loop i
(7)    Search for the faces with the same value of Node_{i,j}.
(8)    Compare the topology of the faces. If two faces have the same nodes list, note them as internal faces.
(9)    All the faces that have not been noted can be stored as the external surfaces.
```

ALGORITHM 2: Recognition of the external surfaces.

(1) $S_5 = S\_all - S_1 - S_2 - S_3 - S_4$
(2)   **for** $i = 1, 2, \ldots, num\_mono - 1$ **do**
(3) $S_6 = ((\text{Surface of elements with } mono\_ID \, [lift\_ID] = i) \wedge (\text{those with } mono\_ID \, [lift\_ID] = i + 1)) \vee S_6$
(4)   **end loop** i
(5)   Recognize all external surfaces of elements with $mono\_ID > 0$, and noted them as S_base.
// Searching for only the base elements based on **Algorithm 2**, that means the foundation faces the dam sits upon will also be included.
(6) $S\_rock = S\_base - S_1$.

ALGORITHM 3: Initial detection of the hole surfaces S_5, transverse joint surfaces S_6, and rock-exposed surfaces S_rock.

TABLE 3: Calculation of solar irradiation.

(a)

Xiluodu Dam	Latitude: 28°13′02″ N	Longitude: 103°33′46″ E
Zhaotong Station	Latitude: 27°19′48″ N	Longitude: 103°45′00″ E

(b)

	Jan 21st	Feb 21st	Mar 21st	Apr 21st	May 21st	Jun 21st
D	21	52	80	111	141	172
η_{Beam}	0.362	0.369	0.448	0.479	0.525	0.504
η_{Diff}	2.080	2.084	1.835	1.791	1.707	1.820
E^*_{Beam} (W/m^2)	674.24	719.12	750.84	764.69	762.99	758.19
E^*_{Diff} (W/m^2)	189.32	204.92	217.25	223.84	224.33	223.10
$H_{\text{Set}} - H_{\text{Rise}}$ (h)	$18.6 - 8.0 = 10.6$	$19 - 7.7 = 11.3$	$19.2 - 7.3 = 11.9$	$19.5 - 6.7 = 12.8$	$19.8 - 6.3 = 13.5$	$19.9 - 6.2 = 13.8$
$\overline{E_{\text{Beam}}}$ (W/m^2)	466.16	504.89	541.53	551.07	547.52	546.35
$\overline{E_{\text{Diff}}}$ (W/m^2)	132.36	143.80	154.89	158.71	158.28	157.89
$\overline{E^V_{\text{Sun}}}$ (W/m^2)	401.51	360.70	280.32	162.93	91.00	71.70
$\overline{E^H_{\text{Sun}}}$ (W/m^2)	378.29	448.80	521.64	561.99	568.09	568.47
	Jul 21st	Aug 21st	Sep 21st	Oct 21st	Nov 21st	Dec 21st
D	202	233	264	294	325	355
η_{Beam}	0.512	0.546	0.487	0.448	0.391	0.365
η_{Diff}	1.820	1.708	1.833	1.883	2.025	2.076
E^*_{Beam} (W/m^2)	751.02	754.78	740.12	707.95	667.55	650.57
E^*_{Diff} (W/m^2)	222.60	220.96	214.20	201.56	187.34	181.68
$H_{\text{Set}} - H_{\text{Rise}}$ (h)	$19.9 - 6.5 = 13.4$	$19.6 - 6.7 = 12.9$	$19 - 6.9 = 12.1$	$18.4 - 7.2 = 11.2$	$18.1 - 7.6 = 10.5$	$18.2 - 7.9 = 10.3$
$\overline{E_{\text{Beam}}}$ (W/m^2)	547.62	539.21	526.69	498.23	463.08	446.57
$\overline{E_{\text{Diff}}}$ (W/m^2)	158.32	155.75	150.59	142.10	131.67	129.80
$\overline{E^V_{\text{Sun}}}$ (W/m^2)	89.61	157.91	270.12	360.71	401.60	407.44
$\overline{E^H_{\text{Sun}}}$ (W/m^2)	568.91	550.41	507.16	441.23	375.37	348.70

5.4. Instrument Setup.

A number of digital thermometers are embedded 0.10 m under the dam surfaces to monitor the concrete surface temperature distribution. Pairs of thermometers are arranged at the same elevation in the same concrete lift: one at the upstream surface and the other at the downstream surface. Monoliths number 6, number 9, number 16, number 22, and number 27 are selected as monitoring sections. Figure 11 shows the instrument layout of the upstream surface of the dam.

5.5. Material Properties.

A double exponent hydration model [38] of concrete is applied in this engineering, which can be expressed as

$$\theta = \theta_0 \left[s \left(1 - e^{-m_1 \tau}\right) + (1 - s)\left(1 - e^{-m_2 \tau}\right) \right], \qquad (36)$$

where θ is the adiabatic temperature rise and θ_0, s, m_1, and m_2 are the fitting parameters. The technical reports of the material experiments reveal that three main types of concrete
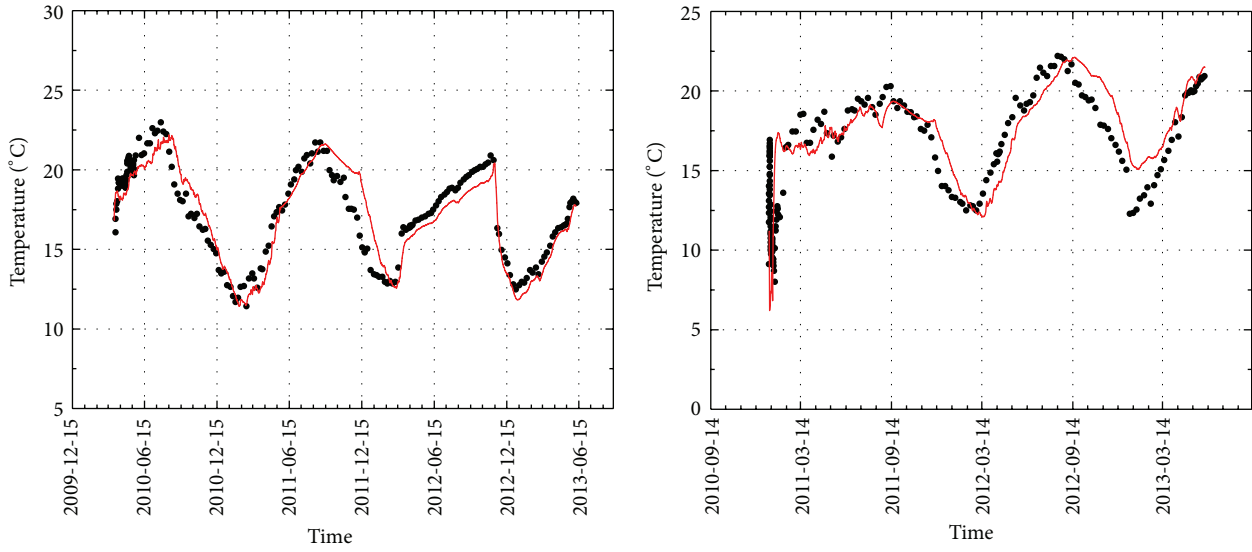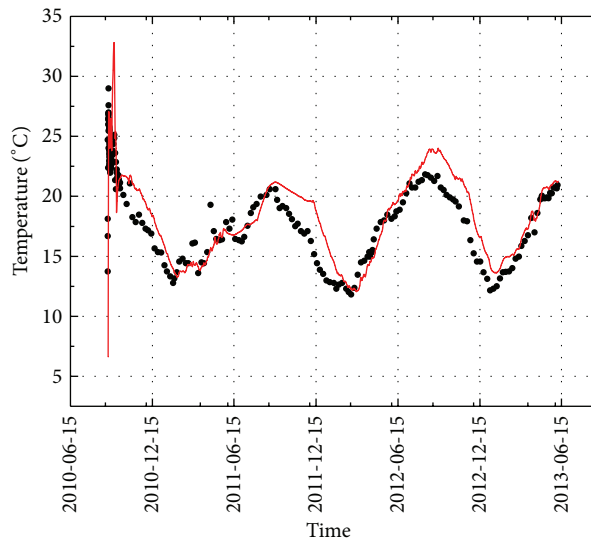
(a) *mono_ID* = 16, elevation = 358.0

(b) *mono_ID* = 22, elevation = 387.7

(c) *mono_ID* = 16, elevation = 403.7

FIGURE 14: Simulation results.

are used in the dam construction. The material properties are listed in Table 4.

5.6. Simulation Model. The 3D dam-foundation system is discretized into hexahedral meshes. A total of 154,008 elements represent the dam body, and 28,026 elements represent the foundation. The total number of nodes is 216,837. The FE mesh layout of the dam body is shown in Figure 12.

6. Results and Discussions

6.1. Surface Taxonomy. The surface procedure mentioned in this study is implemented as a preprocessing facility. The surface groups classified at each step are stored. Figure 13 shows the results of the surface taxonomy map at the 500th and 700th steps, in which different colors represent different surface groups. The FE model is split along the central river to show clearly the upstream and downstream faces. The

(a) June 2011   (b) July 2011   (c) August 2011   (d) September 2011   (e) October 2011

(f) November 2011   (g) December 2011   (h) January 2012   (i) February 2012

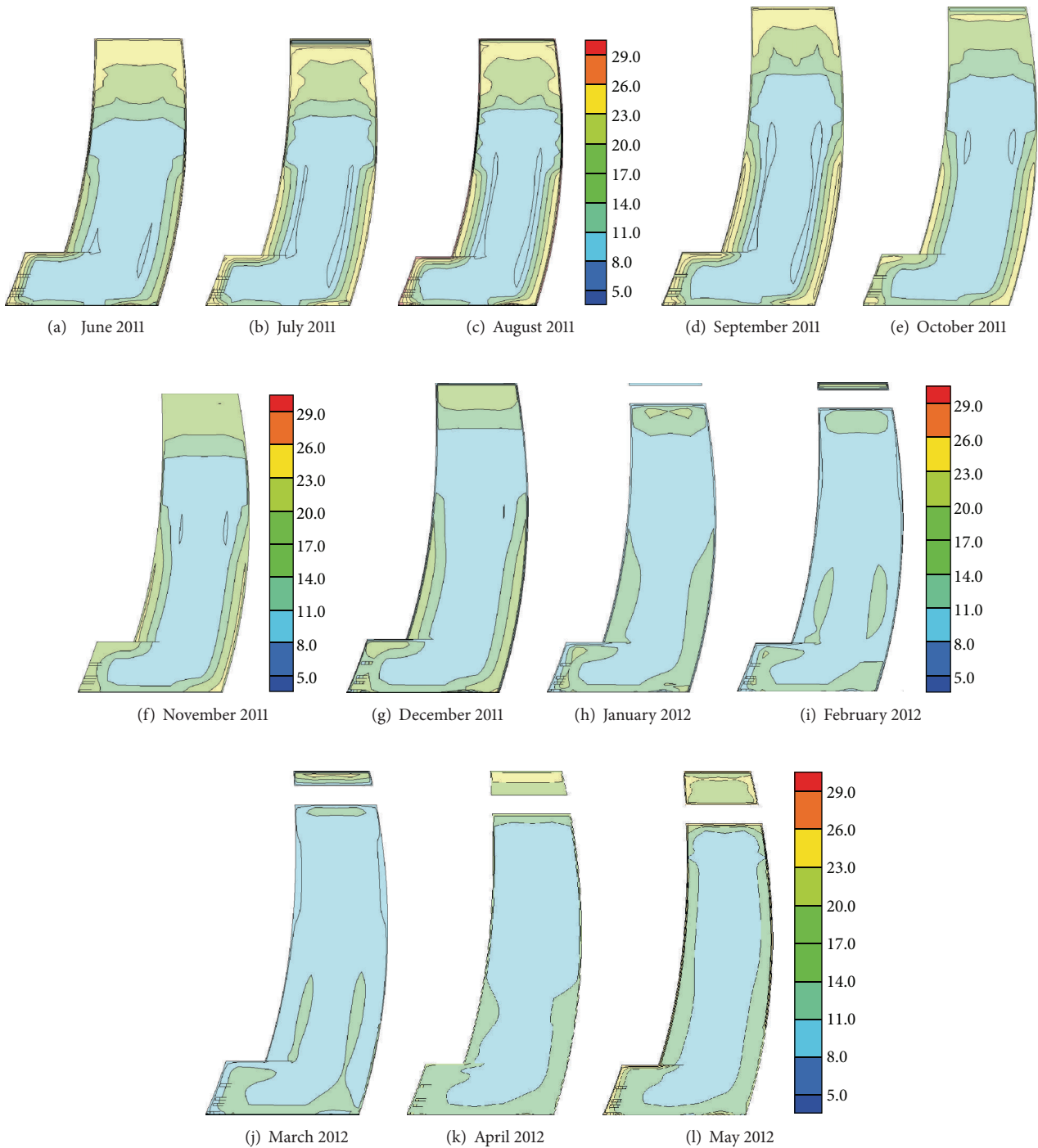(j) March 2012   (k) April 2012   (l) May 2012

FIGURE 15: Temperature contour of the section in monolith 15 throughout a year from June 2011 to May 2012.

external surfaces are correctly extracted. The surface groups by the automatic Boolean-based algorithms are reasonable.

6.2. Verification. The calculation temperature history of nodes that are near the positions of the embedded thermometers is extracted by the program and compared with the monitored data. It is found that they have a good agreement, which verifies the correctness of the external heat transfer

analysis method present in this study. Three thermometers are picked out as shown in Figure 14.

6.3. Temperature Distribution. The simulation result is automatically transported into Tecplot to draw the temperature contour, as mentioned in Section 4.4. Figure 15 shows the temperature section of monolith 15 through a whole year

TABLE 4: Material properties of concrete.

Material property		Type I	Type II	Type III
Basic heat transfer	C_p (J/kg·°C)	943.0	934.0	860.0
	ρ (kg/m³)	2663	2663	2663
	λ (W/m·°C)	2.14	2.14	2.14
Hydration model	θ_0 (°C)	26.3	25.5	24.7
	m_1	0.252	0.252	0.252
	m_2	0.025	0.025	0.025
	s	0.6	0.6	0.6
Radiation	F_r	0.88	0.88	0.88
Air-side convection	a	0.99	0.99	0.99
	b	0.21	0.21	0.21
	m	1.0	1.0	1.0
Solar input	ζ	0.50	0.50	0.50
	g for upstream	0.07	0.07	0.07
	g for downstream	0.20	0.20	0.20
Protection	λ_p for quilt covers (W/m·°C)	0.045	0.045	0.045
	λ_p for PFP boards (W/m·°C)	0.036	0.036	0.036

from June 2011 to May 2012. Conclusions can be drawn from these contour maps as follows.

(i) External thermal flux has great impact on the area underneath the boundary surfaces, for the temperature varies following the seasonal change.

(ii) The arch dam seals the joint layer by layer and starts cooling the sealed regions before the sealing time. We can see that the weather-affected border is obviously narrow in some lifts because of the strong internal cooling source, like (d)~(f) in the figure.

(iii) The after-sealed internal concrete, located a particular height below the top elevation, is not sensitive to the external weather. The temperature does not change much throughout a whole year.

(iv) The surface temperature gradient is more obvious in summer than in winter, for the dam's sealing temperature is 13°C, much lower than the average summer air temperature and closer to the average winter air temperature.

(v) The new-cast lift can reach a relatively high temperature peak due to the hydration reaction and induce a temperature gradient with the old concrete and the external surfaces.

(vi) The ground temperature has impact on the footing region where the temperature is higher than the sealing temperature.

(vii) The upstream face regions which contact with water are mainly affected by the water temperature after March 2012, when the reservoir starts impounding, like (j)~(i) in the figure.

(viii) The blank area is the outlet hole, like (h)~(i) in the figure. The hollow hole makes the hole wall contact with the air, which generates a temperature gradient near the surface.

7. Conclusions

The external heat transfer of dams during the construction phase is complex because such transfer is location specific and time varying. A sound model for the external heat transfer of dams during construction is developed in this study. First, a mathematical model of five external thermal flux factors, namely, air-side convection, electromagnetic radiation, absorbed solar input, water-side convection, and surface insulation effect, is proposed. A surface procedure for FE analysis is also established based on Boolean operations. The proposed procedure can extract external surfaces and can create a taxonomy of surfaces for proper boundary conditions. An arch dam that is under construction in China with a height of 285 m is used to test the proposed method. The method can precisely extract the external surface and can correctly classify these surfaces in each step. The numerical result is compared with the monitoring temperatures. The result shows good agreement, thereby verifying the validity of the proposed method.

Appendix

Hour angle H is defined as the angular displacement of the sun east or west of the local meridian due to the rotation of the earth. To obtain H, the equation of time should be calculated as follows:

$$ET = 2.2918\,[0.0075 + 0.1868\cos\Gamma - 3.2077\sin\Gamma$$
$$-1.4615\cos(2\Gamma) - 4.089\sin(2\Gamma)]\,, \tag{A.1}$$

where ET is expressed in minutes and

$$\Gamma = 360°\,\frac{D-1}{365}. \tag{A.2}$$

Then the apparent solar time (AST) can be expressed in the following equation:

$$AST = \frac{LST + ET/60 + (LON - LSM)}{15}, \qquad (A.3)$$

where LST is the local standard time, decimal hours, LSM is the longitude of local standard time meridian, positive for east, and LON is the longitude of site. For example, China mainland's LSM is 120.

Finally the hour angle H can be given by

$$H = 15\,(AST - 12). \qquad (A.4)$$

A remark is notable that when $H = 0$, β reaches the daily maximum angle of $\pi/2 - |L - \delta|$, the very moment which is called the *solar noon*.

Nomenclature

T: Temperature (°C)
C_p: Specific heat (J/kg·°C)
q: External heat flux (W/m²)
q_c: Air-side convection heat exchange rate (W/m²)
q_a: Absorbed solar irradiation heat flux (W/m²)
q_p: Heat exchange rate through the protection (W/m²)
q_r: Radiative electromagnetic heat flux (W/m²)
q_w: Water-side convection heat flux (W/m²)
h_c: Air-side convection coefficient (W/m²°C)
n: Normal direction
F_r: Emissivity of surface
T_a: Ambient temperature (°C)
V_w: Wind speed (m/s)
N: The normal direction to the surface
f: Internal heat source per unit volume (W/m³)
a: Empirical parameter in (4)
b: Empirical parameter in (4)
m: Empirical parameter in (4)
T_1:   Measured air temperature 1 (°C)
T_2:   Measured air temperature 2 (°C)
H_1:   Measured time 1 (h)
H_2:   Measured time 2 (h)
H_{Mean}:   The middle hour of day between the temperature peak and valley (h)
T_{Max}:   Maximum temperature of a year (°C)
T_{Min}:   Minimum temperature of a year (°C)
D_{Anu}:   The middle day between T_{Max} and T_{Min} (d)
T_{Anu}:   Mean temperature throughout a year (°C)
C: Heat capacity matrix
K: Thermal conductivity matrix
Q: Heat flux vector
V: 3D domain space of FEM
$[K]$:   Symbol for degree Kelvin
$[°C]$:   Symbol for degree Celsius
H: Hour angle (°)
L: Latitude angle (°)
b_p: The width of each protection (m)
E_{Sun}:   The total solar energy input reaching the structure surface (W/m²)
E_{Beam}:   Beam (direct) component of solar radiation (W/m²)
E_{Diff}:   Diffuse component of solar radiation (W/m²)
E_{Refl}:   Ground reflector component of solar radiation (W/m²)
Y_{Beam}:   Irradiation coefficient of the beam component
Y_{Diff}:   Irradiation coefficient of the diffuse component
E_0:   Extraterrestrial solar radiant flux (W/m²)
m: The relative air mass
g: Ground reflectance factor of foreground
E_{sc}:   Solar constant (W/m²)
h_w: Water-side convection coefficient between (W/m²°C)
T_w: Water temperature (°C)
H_{Rise}:   Sunrise hour (h)
H_{Set}:   Sunset hour (h).

Greek Symbols

ρ: Density (kg/m³)
λ: Thermal conductivity (W/m·°C)
τ: Time (s)
η: Parameter representing optical depths
ζ: Absorptivity of the exposed surface
λ_p: The conduction coefficient of each protection (W/m·°C)
ψ: Surface azimuth (°)
σ: Stefan-Boltzmann constant (W m⁻² K⁻⁴)
μ: Inclination angle of the structure surface (°)
γ: The surface-solar azimuth angle (°)
β: Solar altitude angle (°)
ϕ: Solar azimuth angle (°)
θ: Angle of incidence (°).

Acknowledgments

References

[1] J. M. Crow, "The concrete conundrum," *Chemistry World*, vol. 5, no. 3, pp. 62–66, 2008.

[2] Y. Wu and R. Luna, "Numerical implementation of temperature and creep in mass concrete," *Finite Elements in Analysis and Design*, vol. 37, no. 2, pp. 97–106, 2001.

[3] F.-J. Ulm and O. Coussy, "What is a "massive" concrete structure at early ages? Some dimensional arguments," *Journal of Engineering Mechanics*, vol. 127, no. 5, pp. 512–522, 2001.

[4] R. R. Wertz, "Special report: three gorges dam project. Exploring Chinese history," 2011, http://www.ibiblio.org/chinesehistory/contents/07spe/specrep01.html.

[5] H. Demir, "Experimental and numerical studies of natural convection from horizontal concrete cylinder heated with a cylindrical heat source," *International Communications in Heat and Mass Transfer*, vol. 37, no. 4, pp. 422–429, 2010.

[6] Y. Lee, M.-S. Choi, S. T. Yi, and J. K. Kim, "Experimental study on the convective heat transfer coefficient of early-age concrete," *Cement and Concrete Composites*, vol. 31, no. 1, pp. 60–71, 2009.

[7] G. F. Jones and R. W. Jones, "Steady-state heat transfer in an insulated, reinforced concrete wall: theory, numerical simulations, and experiments," *Energy and Buildings*, vol. 29, no. 3, pp. 293–305, 1999.

[8] P. Léger and S. Seydou, "Seasonal thermal displacements of gravity dams located in northern regions," *Journal of Performance of Constructed Facilities*, vol. 23, no. 3, pp. 166–174, 2009.

[9] P. Léger and M. Leclerc, "Hydrostatic, temperature, time-displacement model for concrete dams," *Journal of Engineering Mechanics*, vol. 133, no. 3, pp. 267–277, 2007.

[10] F. Sheibany and M. Ghaemian, "Effects of environmental action on thermal stress analysis of karaj concrete arch dam," *Journal of Engineering Mechanics*, vol. 132, no. 5, pp. 532–544, 2006.

[11] F. Jin, Z. Chen, J. Wang, and J. Yang, "Practical procedure for predicting non-uniform temperature on the exposed face of arch dams," *Applied Thermal Engineering*, vol. 30, no. 14-15, pp. 2146–2156, 2010.

[12] M. Cervera, J. Oliver, and T. Prato, "Simulation of construction of RCC dams. I: temperature and aging," *Journal of Structural Engineering*, vol. 126, no. 9, pp. 1053–1060, 2000.

[13] Y. Chen, C. Wang, S. Li, R. Wang, and J. He, "Simulation analysis of thermal stress of RCC dams using 3-D finite element relocating mesh method," *Advances in Engineering Software*, vol. 32, no. 9, pp. 677–682, 2001.

[14] J. Yang, Y. Hu, Z. Zuo, F. Jin, and Q. Li, "Thermal analysis of mass concrete embedded with double-layer staggered heterogeneous cooling water pipes," *Applied Thermal Engineering*, vol. 35, no. 1, pp. 145–156, 2012.

[15] R. Luna and Y. Wu, "Simulation of temperature and stress fields during RCC dam construction," *Journal of Construction Engineering and Management*, vol. 126, no. 5, pp. 381–388, 2000.

[16] A. Saetta, R. Scotta, and R. Vitaliani, "Stress analysis of concrete structures subjected to variable thermal loads," *Journal of Structural Engineering*, vol. 117, no. 2, pp. 446–457, 1991.

[17] Z. Zuo, Y. Hu, Y. Duan, and J. Yang, "Simulation of the temperature field in mass concrete with double layers of cooling pipes during construction," *Journal of Tsinghua University*, vol. 52, no. 2, pp. 186–228, 2012 (Chinese).

[18] J. Noorzaei, K. H. Bayagoob, W. A. Thanoon, and M. S. Jaafar, "Thermal and stress analysis of kinta RCC dam," *Engineering Structures*, vol. 28, no. 13, pp. 1795–1802, 2006.

[19] J. Noorzaei, K. H. Bayagoob, A. A. Abdulrazeg, M. S. Jaafar, and T. A. Mohammed, "Three dimensional nonlinear temperature and structural analysis of roller compacted concrete dam," *Computer Modeling in Engineering and Sciences*, vol. 47, no. 1, pp. 43–60, 2009.

[20] Z. Zuo, Y. Hu, Q. Li et al., "User-friendly thermal-stress coupled simulating platform of mass concrete," *Chinese Journal of Computational Mechanics*, vol. 30, no. S1, pp. 1–6, 2013 (Chinese).

[21] A. I. H. Malkawl, S. A. Mutasher, and T. J. Qiu, "Thermal-structural modeling and temperature control of roller compacted concrete gravity dam," *Journal of Performance of Constructed Facilities*, vol. 17, no. 4, pp. 177–187, 2003.

[22] Y. A. Cengel, *Heat and Mass Transfer: A Practical Approach*, McGraw-Hill, Boston, Mass, USA, 3rd edition, 2007.

[23] J. A. Palyvos, "A survey of wind convection coefficient correlations for building envelope energy systems' modeling," *Applied Thermal Engineering*, vol. 28, no. 8-9, pp. 801–808, 2008.

[24] Y. Lee, M.-S. Choi, S.-T. Yi, and J.-K. Kim, "Experimental study on the convective heat transfer coefficient of early-age concrete," *Cement and Concrete Composites*, vol. 31, no. 1, pp. 60–71, 2009.

[25] Y. Ballim, "A numerical model and associated calorimeter for predicting temperature profiles in mass concrete," *Cement and Concrete Composites*, vol. 26, no. 6, pp. 695–703, 2004.

[26] NIST. The NIST Reference on Constants, Units, and Uncertainty. 2011.

[27] ASHRAE, *ASHRAE 2009 Fundamentals*, Ashrae Handbook Series, Publications Traffic Administrator, Atlanta, Ga, USA, 2009.

[28] M. Iqbal, *An Introduction to Solar Radiation*, Academic Press, Toronto, Canada, 1983.

[29] F. Kasten and A. T. Young, "Revised optical air mass tables and approximation formula," *Applied Optics*, vol. 28, no. 22, pp. 4735–4738, 1989.

[30] D. Thevenard and K. Haddad, "Ground reflectivity in the context of building energy simulation," *Energy and Buildings*, vol. 38, no. 8, pp. 972–980, 2006.

[31] Y. Shiming, *Heat Transfer*, Higher Education Press, Beijing, China, 1998 (Chinese).

[32] W. S. Janna, *Engineering Heat Transfer*, CRC Press, New York, NY, USA, 2000.

[33] B.-F. Zhu, "Prediction of water temperature in reservoirs," *Journal of Hydraulic Engineering*, vol. 16, no. 2, pp. 12–21, 1985 (Chinese).

[34] S. C. Chapra, *Surface Water-Quality Modeling*, Waveland Press, Long Grove, Ill, USA, 1997.

[35] X. F. Zhang, S. Y. Li, Y. L. Li, Y. Ge, and H. Li, "Effect of superficial insulation on roller-compacted concrete dams in cold regions," *Advances in Engineering Software*, vol. 42, no. 11, pp. 939–943, 2011.

[36] USDOE, "Buried treasure: the environmental, economic, and employment benefits of geothermal energy," in *Geothermal Technologies Program*, Department of Energy, 2004.

[37] MSC Software Corporation, *Theory and User Information*, vol. A, MSC Software Corporation, Newport Beach, Calif, USA, 2012.

[38] B.-F. Zhu, "Compound exponential formula for variation of thermal and mechanical properties with age of concrete," *Journal of Hydraulic Engineering*, vol. 42, no. 1, pp. 1–7, 2011 (Chinese).